RESEARCH ARTICLE

Key Points:
- Analytical derivation of complex frequency-dependent magnetic field on the surface of a metal cylinder in a layered medium
- Analytical solution of the fundamental problem in EM wave propagation well logging
- Analysis and computation of the pole spectra and associated waveguide modes in a cylindrically layered dissipative medium

Derivation of the magnetic field on a metal cylinder excited by a longitudinal magnetic dipole transmitter: II. Cylinder in a two-layer dissipative dielectric medium

Robert Freedman[1]

[1]Schlumberger, Sugar Land, Texas, USA

Abstract We derive an exact convergent analytical solution for the complex frequency-dependent magnetic field on the surface of an infinitely long and perfectly conducting metal cylinder situated in a cylindrically layered dissipative medium. The inhomogeneous medium consists of two exterior cylindrical layers that are concentric with the cylinder. The magnetic field on the cylinder is excited by a longitudinally oriented oscillating magnetic dipole transmitter on the cylinder surface. An exact analytical solution to this problem has not been previously published and is of theoretical as well as practical importance, e.g., in modeling the responses of electromagnetic wave propagation well logging tools. It is shown that the magnetic field on the cylinder surface can be expressed as a real-axis integral; however, the integrand oscillates rapidly and diverges for large values of the integration variable. The real-axis integral is replaced by the sum of two convergent branch line integrals and a sum over the residues of the complex poles in the integrand of the real-axis integral. The poles correspond physically to waveguide modes that propagate with discrete wave numbers. A pole search algorithm is developed to locate the positions of the poles and compute their residues. Phase shifts and attenuations of the magnetic field between receivers for a 1.1 GHz well logging tool are computed to elucidate the pole spectra and the relative contributions of the waveguide modes and the branch cut integrals for different thicknesses of the innermost dielectric layer and for different layer properties.

1. Introduction

The present paper builds on and extends the recent work of *Freedman* [2015], which published the first exact analytical and easily computable solutions for magnetic fields on a metal cylinder excited by both longitudinal and transverse magnetic dipole transmitters on its surface for a cylinder in a *homogeneous* dissipative dielectric medium. In this paper we confront the more challenging problem, and the one of greater theoretical as well as practical importance, e.g., in the computation of the responses of electromagnetic (EM) wave propagation well logging tools [e.g., *Hizem et al.*, 2008], where the devices are situated in an inhomogeneous cylindrically layered medium. We shall consider the theoretical model shown in Figure 1, which consists of a perfectly conducting metal cylinder and two exterior dissipative dielectric cylindrical layers with a longitudinally oriented oscillating point magnetic dipole on the surface of the cylinder. The innermost layer is denoted by medium 1 and is defined in the region $a < r < b$. The radially unbounded outer layer is denoted by medium 2 and is defined for $b < r < \infty$. The thickness of layer 1 is $b - a$. The two-layer problem is important for modeling logging tool responses because frequently, there is a lossy medium (e.g., drilling mud or filter cake on the borehole wall) separating the drill collar or antenna pad from direct contact with the subterranean rock formations.

We derive a real-axis integral solution for $H_z(a, \phi, z)$ from a linear combination of the EM fields derived from magnetic and electric Hertz potentials. The real-axis integral satisfies the boundary conditions and represents a correct formal solution to the boundary-value problem; however, it is not useful for practical computations because the integrand oscillates rapidly and diverges for large values of the integration variable. *Wait* [1987] derived an analytical real-axis integral solution for a related EM well logging problem and noted that the integrand had convergence issues but he did not attempt to confront the technical difficulties required to derive a convergent solution that can be used for practical computations. Using a judiciously chosen branch cut and Cauchy's residue theorem, it is shown that the real-axis integral for $H_z(a, \phi, z)$ can be replaced by a sum of two convergent branch line integrals and a summation over residues from complex poles in the real-axis integrand. We discuss the location and distribution of the poles in the complex plane and provide a pole search algorithm for locating the poles and computing their residues. Two numerical tests used to validate the pole
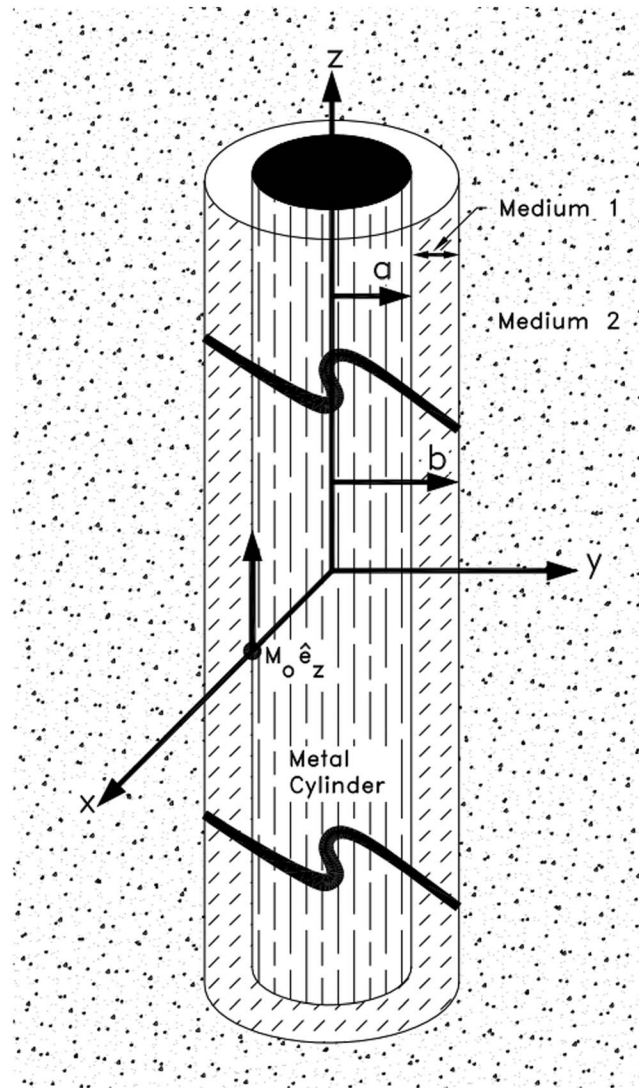
Figure 1. Schematic of the model showing a longitudinally oriented point magnetic dipole transmitter located on the surface of a metal cylinder of radius a. The metal cylinder is situated in a medium consisting of two concentric cylindrical layers. The innermost layer (medium 1) is referred to as the standoff layer. The thickness of the standoff layer 1 is $b - a$. The outermost layer is radially unbounded.

search algorithm and the residue summations are discussed. As a practical example by using the analytical solution, phase shifts and attenuations of the magnetic field between receivers for a 1.1 GHz EM wave propagation well logging tool are computed. The relative contributions of the waveguide modes and the branch cut integral for different thicknesses of the innermost dielectric layer and for different layer properties are discussed.

2. Derivation of the Real-Axis Integral Solution

2.1. Problem Geometry

The cylinder is embedded in a nonmagnetic dissipative dielectric medium that consists of two concentric cylindrical layers with complex propagation constants k_1 and k_2. The standoff layer has propagation constant k_1. The standoff layer separates the cylinder from the radially unbounded outermost layer, which has propagation constant k_2. The geometry and EM properties of the two-layer medium are described by the equation

$$k = \begin{cases} k_1, & \text{if } a \leq r \leq b \\ k_2, & \text{if } b < r \leq \infty \end{cases}, \quad (1)$$

where r is the radial coordinate in the cylindrical coordinate system, a is the cylinder radius, and b is the outer radius of the standoff layer. The thickness of the standoff layer is $b - a$. The EM properties of the layers are described by the complex propagation constants $k_j = \omega\sqrt{\mu_o \varepsilon_j}$ for $j = 1,2$. The complex permittivity of each medium is given by $\varepsilon_j = \varepsilon_o \kappa_j (1 + i \tan \delta_j)$. In these equations ε_o and μ_o are the dielectric permittivity and magnetic susceptibility of a vacuum, respectively, κ_j are the relative dielectric constants, $\tan \delta_j$ are the loss tangents, $\omega = 2\pi f$ is the angular frequency of the oscillating magnetic dipole transmitter, and $i = \sqrt{-1}$. The voltage induced in a magnetic dipole receiver located at (a, ϕ, z) on the cylinder surface is proportional to $H_z(a,\phi,z)$. The EM fields are determined by solving Maxwell's equations, with appropriate boundary conditions, in the region $a \leq r \leq \infty$ for a longitudinally oriented magnetic dipole transmitter located at $(r_o, 0, 0)$. The radial coordinate r_o of the transmitter is chosen to be in the interval $a < r_o < b$ so that the source is initially not on the boundary at $r = a$. The limit $r_o \to a$ is taken in the radial Green's function after the boundary conditions are satisfied. This procedure avoids problems that can occur when the source is on a layer boundary and proper care is not taken to account for the discontinuity of the radial Green's function at the source position.

2.2. Hertz Potentials

The addition of cylindrical layering produces scattering at the layer boundaries. The radial layers destroy the symmetry needed (translational invariance in the radial direction) for pure transverse electric (TE) modes. The

solution of the model in a cylindrically layered medium therefore involves nonzero components for all of the EM field components. If only the EM fields from the magnetic Hertz potential are used, it is not possible to satisfy the boundary conditions in a multilayered cylindrical geometry. The most general solution possible for this geometry can be found from a superposition of the partial fields derived from electric and magnetic Hertz vectors [*Stratton*, 1941]. Thus, we introduce the magnetic Hertz vector $\vec{\Pi}^{(m)} = \left(0, \ 0, \ \Pi_z^{(m)}\right)$, which in cylindrical coordinates (r, ϕ, z) satisfies the inhomogeneous scalar Helmholtz wave equation (1) given in *Freedman* [2015] for a point magnetic dipole transmitter with dipole moment M_o oriented along the z-direction with coordinates $(r_o, 0, 0)$. The EM fields generated by $\Pi_z^{(m)}$ are TE waves with $E_z = 0$. The boundary conditions can be satisfied by a superposition of the partial EM fields derived from $\Pi_z^{(m)}$ and those derived from the electric Hertz vector $\vec{\Pi}^{(e)} = \left(0, \ 0, \ \Pi_z^{(e)}\right)$, which satisfies the homogeneous Helmholtz wave equation.

The EM fields derived from $\Pi_z^{(e)}$ are transverse magnetic waves with $H_z = 0$. The two partial differential equations for the Hertz potentials are solved in section 2.4 subject to the boundary conditions discussed in the next section.

2.3. EM Fields and Boundary Conditions

The electric and magnetic fields computed from the *magnetic* Hertz vector are given by

$$\vec{E}^{(m)} = i\omega\mu_o \nabla \times \vec{\Pi}^{(m)} \tag{2a}$$

and

$$\vec{H}^{(m)} = \nabla \times \nabla \times \vec{\Pi}^{(m)}. \tag{2b}$$

The electric and magnetic fields computed from the *electric* Hertz vector are given by

$$\vec{E}^{(e)} = \nabla \times \nabla \times \vec{\Pi}^{(e)} \tag{3a}$$

and

$$\vec{H}^{(e)} = \frac{-ik^2}{\omega\mu_o} \nabla \times \vec{\Pi}^{(e)}. \tag{3b}$$

The boundary conditions are satisfied by the *total* fields

$$\vec{E}^{(t)} = \vec{E}^{(m)} + \vec{E}^{(e)} \tag{4a}$$

and

$$\vec{H}^{(t)} = \vec{H}^{(m)} + \vec{H}^{(e)}. \tag{4b}$$

The boundary conditions require that the tangential components of the total electric field $E_{1,\phi}^{(t)} = 0$ and $E_{1,z}^{(t)} = 0$ vanish on the surface of the perfectly conducting cylinder at $r = a$. We find from the boundary condition $E_{1,\phi}^{(t)} = 0$ that

$$\left(-i\omega\mu_o \frac{\partial \Pi_{1,z}^{(m)}}{\partial r} + \frac{1}{r}\frac{\partial^2 \Pi_{1,z}^{(e)}}{\partial z \partial \phi}\right)_{r=a} = 0, \tag{5}$$

and from the boundary condition $E_{1,z}^{(t)} = 0$ we find

$$\left(\frac{\partial^2 \Pi_{1,z}^{(e)}}{\partial z^2} + k_1^2 \Pi_{1,z}^{(e)}\right)_{r=a} = 0, \tag{6}$$

where the subscripts $l = 1, 2$ for the EM fields and the Hertz vectors denote the layer indices. The next step is to apply the boundary conditions at the interface separating the two cylindrical layers. The boundary conditions derived from Maxwell's equations require that at $r = b$ the tangential components of $\vec{E}^{(t)}$ and $\vec{H}^{(t)}$ are continuous, which leads to four equations. From the condition that $E_{1,\phi}^{(t)} = E_{2,\phi}^{(t)}$ one finds

$$\left(-i\omega\mu_o \frac{\partial \Pi_{1,z}^{(m)}}{\partial r} + \frac{1}{r}\frac{\partial^2 \Pi_{1,z}^{(e)}}{\partial z \partial \phi}\right)_{r=b} = \left(-i\omega\mu_o \frac{\partial \Pi_{2,z}^{(m)}}{\partial r} + \frac{1}{r}\frac{\partial^2 \Pi_{2,z}^{(e)}}{\partial z \partial \phi}\right)_{r=b}. \tag{7}$$

The condition $E_{1,z}^{(t)} = E_{2,z}^{(t)}$ at $r = b$ gives

$$\left(\frac{\partial^2 \Pi_{1,z}^{(e)}}{\partial z^2} + k_1^2 \Pi_{1,z}^{(e)}\right)_{r=b} = \left(\frac{\partial^2 \Pi_{2,z}^{(e)}}{\partial z^2} + k_2^2 \Pi_{2,z}^{(e)}\right)_{r=b}. \tag{8}$$

The requirement that $H_{1,z}^{(t)} = H_{2,z}^{(t)}$ at $r = b$ leads to the equation

$$\left(\frac{\partial^2 \Pi_{1,z}^{(m)}}{\partial z^2} + k_1^2 \Pi_{1,z}^{(m)}\right)_{r=b} = \left(\frac{\partial^2 \Pi_{2,z}^{(m)}}{\partial z^2} + k_2^2 \Pi_{2,z}^{(m)}\right)_{r=b} \tag{9}$$

and the condition $H_{1,\phi}^{(t)} = H_{2,\phi}^{(t)}$ at $r = b$ leads to

$$\left(\frac{1}{r}\frac{\partial^2 \Pi_{1,z}^{(m)}}{\partial z \partial \phi} + \frac{ik_1^2}{\omega\mu_o}\frac{\partial \Pi_{1,z}^{(e)}}{\partial r}\right)_{r=b} = \left(\frac{1}{r}\frac{\partial^2 \Pi_{2,z}^{(m)}}{\partial z \partial \phi} + \frac{ik_2^2}{\omega\mu_o}\frac{\partial \Pi_{2,z}^{(e)}}{\partial r}\right)_{r=b}. \tag{10}$$

2.4. Solution of the Partial Differential Equations for the Electric and Magnetic Hertz Potentials

To solve the Helmholtz equations, we assume the following expansions for the Hertz potentials:

$$\Pi_{l,z}^{(m)} = \frac{2}{\pi}\sum_{n=0}^{\infty} \varepsilon_n \cos n\phi \int_0^{\infty} \widetilde{\Pi}_{n,l}^{(m)}(\lambda, r)\cos\lambda z \, d\lambda \tag{11}$$

and

$$\Pi_{l,z}^{(e)} = \frac{2}{\pi}\sum_{n=0}^{\infty} \varepsilon_n \sin n\phi \int_0^{\infty} \widetilde{\Pi}_{n,l}^{(e)}(\lambda, r)\sin\lambda z \, d\lambda. \tag{12}$$

We have introduced the Neumann function $\varepsilon_n = \delta_{n,0} + 2(1 - \delta_{n,0})$, where $\delta_{n,o}$ is the Kronecker delta function. The solutions in equations (11) and (12) will be shown to satisfy both the partial differential equations and the boundary conditions. Substituting equations (11) and (12) into the Helmholtz wave equations satisfied by $\Pi_{l,z}^{(m)}$ and $\Pi_{l,z}^{(e)}$ respectively, easily finds that the two transformed radial potentials $\widetilde{\Pi}_{n,l}^{(m)}(\lambda, r)$ and $\widetilde{\Pi}_{n,l}^{(e)}(\lambda, r)$ obey Bessel's equation. The magnetic Hertz potential solutions in the domain $a \leq r \leq \infty$ that are regular at infinity can be written in terms of modified Bessel functions:

$$\widetilde{\Pi}_{n,1}^{(m)}(\lambda, r) = A_n K_n(\gamma_1 r) + B_n I_n(\gamma_1 r) + \frac{M_o}{4\pi}K_n(\gamma_1 r_>)I_n(\gamma_1 r_<) \tag{13a}$$

for $a \leq r \leq b$ and

$$\widetilde{\Pi}_{n,2}^{(m)}(\lambda, r) = C_n K_n(\gamma_2 r) \tag{13b}$$

for $r \geq b$. The solutions for the electric Hertz vector are given by

$$\widetilde{\Pi}_{n,1}^{(e)}(\lambda, r) = D_n K_n(\gamma_1 r) + E_n I_n(\gamma_1 r) \tag{13c}$$

for $a \leq r \leq b$ and

$$\widetilde{\Pi}_{n,2}^{(e)}(\lambda, r) = F_n K_n(\gamma_2 r) \tag{13d}$$

for $r \geq b$.

The last term in equation (13a) is the radial Green's function in cylindrical coordinates where in standard notation $r_<(r_>)$ is the lesser (greater) of r and r_o. The functions $I_n(\gamma_l r)$ and $K_n(\gamma_l r)$ are modified Bessel functions and $\gamma_l = \sqrt{\lambda^2 - k_l^2}$. The six unknown coefficients A_n, B_n, C_n, D_n, E_n, and F_n can be determined from solving the set of six linear algebraic equations derived from the boundary conditions.

2.5. Solving for the Unknown Coefficients

This section applies the boundary conditions in equations (5)–(10) by using equations (11) and (12) and equations (13a)–(13d). The boundary conditions lead to a set of six linear algebraic equations for the six unknown coefficients A_n, B_n, C_n, D_n, E_n, and F_n. Because we are interested in calculating $H_z(a, \phi, z)$ on the surface of the

metal cylinder, we only need the two coefficients A_n and B_n; however, they must be determined by solving the full set of six linear equations resulting from application of the boundary conditions. The derivation of the set of six linear equations requires some straightforward but rather tedious algebra. One can show from the set of six equations that E_n and F_n can be determined solely from D_n and that the resulting set of four linear algebraic equations must be solved for the coefficients A_n, B_n, C_n, and D_n. The four equations to be solved after eliminating E_n and F_n are

$$A_n K_n(\gamma_1 b) + B_n I_n(\gamma_1 b) - \frac{\gamma_2^2}{\gamma_1^2} C_n K_n(\gamma_2 b) = -\frac{M_o}{4\pi} K_n(\gamma_1 b) I_n(\gamma_1 a), \tag{14}$$

$$A_n K_n'(\gamma_1 a) + B_n I_n'(\gamma_1 a) = -\frac{M_o}{4\pi} K_n(\gamma_1 a) I_n'(\gamma_1 a), \tag{15}$$

$$A_n K_n'(\gamma_1 b) + B_n I_n'(\gamma_1 b) - \frac{\gamma_2}{\gamma_1} C_n K_n'(\gamma_2 b) + D_n \Lambda_{1n} = -\frac{M_o}{4\pi} K_n'(\gamma_1 b) I_n(\gamma_1 a), \tag{16}$$

and

$$A_n K_n(\gamma_1 b) + B_n I_n(\gamma_1 b) - C_n K_n(\gamma_2 b) + D_n \Lambda_{2n} = -\frac{M_o}{4\pi} K_n(\gamma_1 b) I_n(\gamma_1 a). \tag{17}$$

The primes on the Bessel functions denote derivatives with respect to their arguments. The functions Λ_{1n} and Λ_{2n} in equations (16) and (17), respectively, are defined as follows:

$$\Lambda_{1n} = \frac{in\lambda}{\gamma_1 b \omega \mu_o} \frac{(\gamma_2^2 - \gamma_1^2)}{\gamma_2^2} \frac{F_{1,n}}{I_n(\gamma_1 a)} \tag{18}$$

and

$$\Lambda_{2n} = \frac{i\gamma_1}{(n\lambda \omega \mu_o b)} \frac{Q_n(\lambda)}{I_n(\gamma_1 a)}. \tag{19}$$

We have also defined the quantity Q_n in equation (19)

$$Q_n(\lambda) = (k_1 b)^2 F_{2,n} - \frac{\gamma_1}{\gamma_2} \frac{K_n'(\gamma_2 b)}{K_n(\gamma_2 b)} (k_2 b)^2 F_{1,n}, \tag{20}$$

where

$$F_{1,n} = K_n(\gamma_1 b) I_n(\gamma_1 a) - K_n(\gamma_1 a) I_n(\gamma_1 b) \tag{21}$$

and

$$F_{2,n} = K_n'(\gamma_1 b) I_n(\gamma_1 a) - K_n(\gamma_1 a) I_n'(\gamma_1 b). \tag{22}$$

The next step is to solve the four equations (14)–(17) for the two coefficients A_n and B_n that are needed to calculate the z component of the magnetic field on the cylinder surface. To simplify equations (14)–(22) we let $r_o = a$ so that the dipole source is on the cylinder surface. This has no effect on the ensuing calculations.

On recalling equations (11) and (13a) and also equation (12) in *Freedman* [2015] one finds

$$H_z(a, \phi, z) = \frac{-1}{\pi} \sum_{n=0}^{\infty} \varepsilon_n \cos n\phi \int_{-\infty}^{\infty} \gamma_1^2 \left[A_n K_n(\gamma_1 a) + B_n I_n(\gamma_1 a) + \frac{M_o}{4\pi} K_n(\gamma_1 r_o) I_n(\gamma_1 a) \right] \exp(i\lambda |z|) d\lambda, \tag{23}$$

where we have made use of the fact that the integrand is an even function of λ to extend the integral over the entire real axis. We have also replaced the receiver position z by $|z|$ because it follows from the symmetry of the problem that the EM fields are even functions of z. It is clear from equation (23) that the real-axis integral for the z component of the magnetic field on the cylinder is determined once A_n and B_n are known.

We solve the set of four linear equations (14)–(17) by using Cramer's rule and write A_n and B_n as the ratio of determinants:

$$A_n = \frac{N_{1n}}{\Delta_n} \tag{24a}$$

and

$$B_n = \frac{N_{2n}}{\Delta_n}. \tag{24b}$$

The determinants N_{1n}, N_{2n}, and Δ_n for the system of equations (14)–(17) can easily be evaluated by taking advantage of the zeroes in the first two rows of the fourth column by using cofactors and expanding along column four. Upon recalling equations (18)–(21) and performing some rather lengthy algebra, the determinant of the coefficients can be expressed as

$$\Delta_n = \frac{-in\lambda}{b\omega\mu_o\gamma_1^3\gamma_2^2} \frac{K_n(\gamma_2 b)}{I_n(\gamma_1 a)} \left[(k_1^2 - k_2^2)^2 F_{1,n}F_{3,n} + \frac{\gamma_1^2\gamma_2^2 Q_n}{(n\lambda)^2}\left(\gamma_2^2 F_{4,n} + \frac{\gamma_1\gamma_2 K_n'(\gamma_2 b)F_{3,n}}{K_n(\gamma_2 b)}\right) \right],$$

(25)

where we have defined the two functions

$$F_{3,n} = K_n(\gamma_1 b)I_n'(\gamma_1 a) - I_n(\gamma_1 b)K_n'(\gamma_1 a)$$

(26)

and

$$F_{4,n} = K_n'(\gamma_1 a)I_n'(\gamma_1 b) - I_n'(\gamma_1 a)K_n'(\gamma_1 b).$$

(27)

The next step is to evaluate the terms in the numerator of equation (23). On recalling equations (24a) and (24b) and after evaluating the determinants considerable algebra results in

$$N_{1n}K_n(\gamma_1 a) + N_{2n}I_n(\gamma_1 a) + \frac{M_o}{4\pi}\Delta_n \ I_n(\gamma_1 a)K_n(\gamma_1 a) =$$

$$\frac{iM_o\,n\lambda}{4\pi\omega\mu_o b\gamma_1^4\gamma_2^2 a}\frac{K_n(\gamma_2 b)}{I_n(\gamma_1 a)}\left[(k_1^2 - k_2^2)^2 F_{1,n}^2 - \frac{\gamma_1^2\gamma_2^2 Q_n}{(n\lambda)^2}\left(\gamma_2^2 F_{2,n} - \frac{\gamma_1\gamma_2 K_n'(\gamma_2 b)F_{1,n}}{K_n(\gamma_2 b)}\right) \right].$$

(28)

In arriving at equation (28), we made use of the Wronskian relationship given in equation (15) of *Freedman* [2015] for modified Bessel functions of integer order.

2.6. Real-Axis Integral Representation for $H_z(a,\phi,z)$

Recalling equations (24a) and (24b) and substituting equations (25) and (28) into equation (23) finds that

$$H_z(a, \phi, z) = \frac{M_o}{4\pi^2 a}\sum_{n=0}^{\infty}\varepsilon_n\cos n\phi\int_{-\infty}^{\infty}\frac{N_n(\lambda)}{D_n(\lambda)}\exp(i\lambda|z|)\,d\lambda,$$

(29)

where for $n > 0$:

$$N_n(\lambda) = \gamma_1\left[(k_1^2 - k_2^2)^2 F_{1,n}^2 - \frac{\gamma_1^2\gamma_2^2 Q_n}{(n\lambda)^2}\left(\gamma_2^2 F_{2,n} - \frac{\gamma_1\gamma_2 K_n'(\gamma_2 b)F_{1,n}}{K_n(\gamma_2 b)}\right) \right]$$

(30)

and

$$D_n(\lambda) = (k_1^2 - k_2^2)^2 F_{1,n}F_{3,n} + \frac{\gamma_1^2\gamma_2^2 Q_n}{(n\lambda)^2}\left(\gamma_2^2 F_{4,n} + \frac{\gamma_1\gamma_2 K_n'(\gamma_2 b)F_{3,n}}{K_n(\gamma_2 b)}\right).$$

(31)

For $n = 0$ we find that

$$N_0 = -\gamma_1\left(F_{2,0} - \frac{\gamma_1 K_o'(\gamma_2 b)F_{1,0}}{\gamma_2 K_o(\gamma_2 b)} \right)$$

(32)

and

$$D_0 = F_{4,0} + \frac{\gamma_1 K_o'(\gamma_2 b)F_{3,0}}{\gamma_2 K_o(\gamma_2 b)}.$$

(33)

The real-axis integral representation for the magnetic field given in equation (29) is a formal mathematical solution; however, it is not useful for practical computations. The integrand in equation (29) oscillates rapidly and can be shown by using the asymptotic behavior of the modified Bessel functions [*Olver*, 1965] to increase linearly with λ as $\lambda \to \infty$. This behavior is similar to that of the integrand in the real-axis integral representation of $H_z(a,\phi,z)$ for the one-layer or unbounded homogeneous medium problem, i.e., see equation (16) in *Freedman* [2015].

In the next section we show that equation (29) can be replaced by a sum of two branch line integrals plus the sum of residues of poles in the complex λ-plane. The complex integrands of the branch line integrals are

smooth functions that decay exponentially for large values of the integration variable. The poles in the integrand of the real-axis integral in the complex λ-plane are associated with waveguide or trapped modes that propagate in the first layer at $a \leq r \leq b$.

Before concluding this section, it is important to note that we can show that the real-axis integral in equation (29) reduces to the correct integral representation derived by *Freedman* [2015] for the cylinder in an unbounded medium in the limit representing an unbounded medium by letting $\gamma_1 = \gamma_2 = \gamma$ (or equivalently $k_1 = k_2 = k$). Here $\gamma = \sqrt{\lambda^2 - k^2}$, where k is the complex propagation constant of the unbounded medium. These results follow after some algebra applied to equations (30) and (31) for $n > 0$ and to equations (32) and (33) for $n = 0$ by using equations (21), (22), (26), and (27). The calculations are straightforward if one combines terms and uses the Wronskian relation in equation (15) of *Freedman* [2015]; therefore, to save space we do not display the detailed algebra required to show that equation (29) correctly reduces to equation (16) derived by *Freedman* [2015] for the unbounded medium. It is worth noting that in this limit the radius b of the interface that separates the two media is an irrelevant parameter that cancels out of the calculations as required.

Another important property of the integrand in equation (29) that we use in the next section is that it is an even function of γ_1, and therefore, the integrand is a single-valued function of γ_1 in the complex λ-plane. This is not at all obvious. The algebra to prove this is somewhat tedious but straightforward, and to save space we simply discuss the proof and leave the details to the interested reader. The following analytic continuation formulas for the modified Bessel functions [*Olver*, 1965] are used:

$$I_n\left(e^{i\pi}z\right) = e^{in\pi}I_n(z) \tag{34a}$$

$$K_n\left(e^{i\pi}z\right) = e^{-in\pi}K_n(z). \tag{34b}$$

Using equation (34a) and (34b), first equations (21), (22), (26), and (27) are used to prove that the functions $F_{1,n}$ and $F_{4,n}$ are even in γ_1 and that $F_{2,n}$ and $F_{3,n}$ are odd in γ_1. It then follows that Q_n in equation (20) is an odd function of γ_1. From these results it is easy to show by using equations (30)–(33) that the integrand in equation (29) is a single-valued function of γ_1 in the complex λ-plane, and therefore, the points $\lambda = \pm k_1$ are not branch points of the integrand. This result is consistent with the findings in an important paper by *Chew* [1983], who showed quite generally for the wave equation in a cylindrically multilayered medium with N layers that the only branch point in the integrand is at $\lambda = \pm k_N$, where k_N is the propagation constant of the outermost unbounded layer.

3. Derivation of Convergent Integral Representation and Residue Summation for $H_z(a,\phi,z)$

From the preceding discussion the integrand in equation (29) is an analytic function of λ in the complex λ-plane except for branch points at $\lambda = \pm k_2$ and poles at the zeroes of the denominator, i.e., for $D_n(\lambda) = 0$. Applying Cauchy's residue theorem to the same integration path indicated by the arrows shown in Figure 2 in *Freedman* [2015], where the branch point in the upper half of the λ-plane is at $\lambda = +k_2$, leads to

$$H_z(a, \phi, z) + I_{\gamma_{2+}} + I_{\gamma_{2-}} = 2\pi i \sum_{n=0}^{\infty} \sum_{k} R_n\left(\lambda_n^{(k)}\right), \tag{35}$$

where $\lambda_n^{(k)}$ is the complex coordinate of the kth pole of azimuthal order n of the integrand in equation (29) and $I_{\gamma_{2\pm}}$ are the branch line integrals shown in Figure 2 of *Freedman* [2015]. Note for equation (35) to be valid, the integrand in equation (29) must vanish on the infinite semicircle in the upper half of the λ-plane, which is satisfied provided that $|z| \neq 0$, which is the case of practical interest. The poles are the zeroes of the denominator of the integrand and are the solutions of the transcendental equation:

$$D_n\left(\lambda_n^{(k)}\right) = 0. \tag{36}$$

The solutions of equation (36) were found by using a complex Newton's method and a numerical grid search algorithm in the complex λ-plane, which is discussed in section 4. We have found numerically that for each value of the azimuthal mode number n there can be multiple solutions of equation (36) corresponding to different values of the index k. The index k can be thought of as corresponding to a branch label because

we find that for thick standoff layers, multiple branches roughly resembling families of hyperbolas with each consisting of poles of all azimuthal orders ($n = 0, 1, 2, \ldots$) can exist. $R_n\left(\lambda_n^{(k)}\right)$ are the residues of the poles in the integrand of equation (29), i.e.,

$$R_n\left(\lambda_n^{(k)}\right) = \frac{M_o}{4\pi^2 a} \frac{\varepsilon_n \cos n\phi \, N_n\left(\lambda_n^{(k)}\right) \exp\left(i\lambda_n^{(k)} |z|\right)}{D_n'\left(\lambda_n^{(k)}\right)}, \tag{37}$$

where D_n' is the derivative with respect to λ of equation (31) for $n > 0$ and equation (33) for $n = 0$.

The next step is to consider the two branch line integrals in equation (35). The branch cut discussed in section 2.4 of *Freedman* [2015] leads to branch line integrals $I_{\gamma_{2+}}$ and $I_{\gamma_{2-}}$ with integrands that converge exponentially to zero as the dimensionless integration variable increases. The branch cut separates the two Riemann sheets of the double valued function $\gamma_2 = \sqrt{\lambda^2 - k_2^2}$ in the complex λ-plane. Moreover, on the branch cut Re $\gamma_2 = 0$ and on the two branch lines labeled γ_{2+} and γ_{2-} the complex parameter γ_2 is pure imaginary and has the values

$$\gamma_{2+} = u \exp\left(\frac{i\pi}{2}\right) \tag{38a}$$

and

$$\gamma_{2-} = u \exp\left(-\frac{i\pi}{2}\right). \tag{38b}$$

Next we express γ_1 (which is continuous across the branch cut) in terms of the branch line coordinate u.

$$\gamma_{1+} = \gamma_{1-} = \gamma_1 \equiv \sqrt{\lambda^2 - k_1^2} = \sqrt{k_2^2 - k_1^2 - u^2}. \tag{38c}$$

Applying the branch cut transformations using the same Bessel function transformations discussed in section 2.4 of *Freedman* [2015] to the integrand in equation (29) and introducing the dimensionless integration variable $x = ua$ and the dimensionless z-coordinate $\bar{z} = z/a$ one finds

$$I_{\gamma_{2+}} = \frac{M_o}{4\pi^2 a^3} \sum_{n=0}^{\infty} \varepsilon_n \cos n\phi \int_0^{\infty} \frac{x e^{i\sqrt{(k_2 a)^2 - x^2}|\bar{z}|}}{\sqrt{(k_2 a)^2 - x^2}} \frac{N_n^{(+)}(x)}{D_n^{(+)}(x)} dx. \tag{39}$$

In equation (39) we have defined the following functions for $n > 0$:

$$N_n^{(+)}(x) = t(x)\left[\left[(k_1 a)^2 - (k_2 a)^2\right]^2 \cdot F_{1,n}^2(x) + \frac{ixt^2(x)S_n^{(+)}(x)}{n^2\left[(k_2 a)^2 - x^2\right]} \cdot \left\{x^2 F_{2,n}(x) + \frac{x t(x) H_n^{(2)\prime}\left(\frac{xb}{a}\right) F_{1,n}(x)}{H_n^{(2)}\left(\frac{xb}{a}\right)}\right\}\right], \tag{40}$$

$$D_n^{(+)}(x) = \left[\left[(k_1 a)^2 - (k_2 a)^2\right]^2 \cdot F_{1,n}(x) F_{3,n}(x) - \frac{ixt^2(x)S_n^{(+)}(x)}{n^2\left[(k_2 a)^2 - x^2\right]} \cdot \left\{x^2 F_{4,n}(x) - \frac{x t(x) H_n^{(2)\prime}\left(\frac{xb}{a}\right) F_{3,n}(x)}{H_n^{(2)}\left(\frac{xb}{a}\right)}\right\}\right] \tag{41}$$

and for $n = 0$:

$$N_0^{(+)} = -t(x)\left[F_{2,0}(x) + \frac{t(x) H_0^{(2)\prime}\left(x\frac{b}{a}\right) F_{1,0}(x)}{x H_0^{(2)}\left(x\frac{b}{a}\right)}\right] \tag{42}$$

$$D_0^{(+)} = \left[F_{4,0}(x) - \frac{t(x) H_0^{(2)\prime}\left(x\frac{b}{a}\right) F_{3,0}(x)}{x H_0^{(2)}\left(x\frac{b}{a}\right)}\right]. \tag{43}$$

In equations (42) and (43) we canceled a common multiplicative factor because only the ratio is needed in equation (39). In equations (40)–(43) we used equation (38c) to define the two functions

$$S_n^{(+)}(x) = ix(k_1 b)^2 F_{2,n}(x) + \frac{i t(x) H_n^{(2)\prime}\left(\frac{xb}{a}\right) F_{1,n}(x)(k_2 b)^2}{H_n^{(2)}\left(\frac{xb}{a}\right)} \tag{44}$$

and,

$$t(x) \equiv \gamma_1 a = \sqrt{(k_2 a)^2 - (k_1 a)^2 - x^2}. \tag{45}$$

With the definition of $\gamma_1 a$ in equation (45), it can be seen that $\gamma_1 b = t(x)(b/a)$ so that the arguments of the functions $F_{1,n}$, $F_{2,n}$, $F_{3,n}$, and $F_{4,n}$ defined previously in equations (21), (22), (26), and (27), respectively, are easily transformed, e.g.,

$$F_{1,n}(x) = K_n\left(t(x)\frac{b}{a}\right)I_n(t(x)) - K_n(t(x))I_n\left(t(x)\frac{b}{a}\right). \tag{46}$$

The calculation of the branch line integral I_{γ_2-} in equation (35) is similar to the calculation of I_{γ_2+} and one finds that

$$I_{\gamma_2-} = -\frac{M_o}{4\pi^2 a^3}\sum_{n=0}^{\infty}\varepsilon_n\cos n\phi\int_0^{\infty}\frac{x e^{i\sqrt{(k_2a)^2-x^2}|\bar{z}|}}{\sqrt{(k_2a)^2-x^2}}\frac{N_n^{(-)}(x)}{D_n^{(-)}(x)}dx, \tag{47}$$

which has a form similar to the result for I_{γ_2+} in equation (39). The difference in the algebraic sign of the common multiplicative factors in equations (39) and (47) arises because the limits of the two branch line integrals are reversed. In equation (47) we defined the following for $n > 0$:

$$N_n^{(-)}(x) = t(x)\left[\left[(k_1a)^2-(k_2a)^2\right]^2\bullet F_{1,n}^2(x) + \frac{ixt^2(x)S_n^{(-)}(x)}{n^2\left[(k_2a)^2-x^2\right]}\bullet\left\{x^2F_{2,n}(x) + \frac{xt(x)H_n^{(1)'}\left(\frac{xb}{a}\right)F_{1,n}(x)}{H_n^{(1)}\left(\frac{xb}{a}\right)}\right\}\right], \tag{48}$$

and

$$D_n^{(-)}(x) = \left[\left[(k_1a)^2-(k_2a)^2\right]^2\bullet F_{1,n}(x)F_{3,n}(x) - \frac{ixt^2(x)S_n^{(-)}(x)}{n^2\left[(k_2a)^2-x^2\right]}\bullet\left\{x^2F_{4,n}(x) - \frac{xt(x)H_n^{(1)'}\left(\frac{xb}{a}\right)F_{3,n}(x)}{H_n^{(1)}\left(\frac{xb}{a}\right)}\right\}\right], \tag{49}$$

and for $n = 0$:

$$N_0^{(-)}(x) = -t(x)\left[F_{2,0}(x) + \frac{t(x)H_0^{(1)'}\left(\frac{xb}{a}\right)F_{1,0}(x)}{xH_0^{(1)}\left(\frac{xb}{a}\right)}\right], \tag{50}$$

and

$$D_0^{(-)}(x) = F_{4,0}(x) - \frac{t(x)H_0^{(1)'}\left(\frac{xb}{a}\right)F_{3,0}(x)}{xH_0^{(1)}\left(\frac{xb}{a}\right)}, \tag{51}$$

where

$$S_n^{(-)}(x) = ix(k_1b)^2F_{2,n}(x) + \frac{it(x)H_n^{(1)'}\left(\frac{xb}{a}\right)F_{1,n}(x)(k_2b)^2}{H_n^{(1)}\left(\frac{xb}{a}\right)}. \tag{52}$$

In equations (50) and (51) we canceled a common multiplicative factor because only the ratio is needed in equation (47). Comparing equations (39)–(44) with equations (47)–(52) shows that the only differences in the integrands of the two branch line integrals are in the factors that depend on γ_2. This is exactly as expected because γ_2 is a branch point. It assumes opposite signs on the two branch lines, whereas factors involving γ_1 are the same on both branch line integrals because the integrands are single valued functions of γ_1 on both the upper and lower Riemann sheets.

Assembling these results and recalling equation (35) enables writing the z component of the magnetic field $H_z(a, \phi, z)$ valid everywhere on the cylinder except at $|\bar{z}| = 0$ in the following form:

$$H_z(a,\phi,z) = -\frac{M_o}{4\pi^2a^3}\left[\begin{array}{l}\displaystyle\sum_{n=0}^{\infty}\varepsilon_n\cos n\phi\int_0^{\infty}\frac{x\exp\left(i\sqrt{(k_2a)^2-x^2}|\bar{z}|\right)}{\sqrt{(k_2a)^2-x^2}}\left(\frac{N_n^{(+)}(x)}{D_n^{(+)}(x)} - \frac{N_n^{(-)}(x)}{D_n^{(-)}(x)}\right)dx \\[12pt] \displaystyle -2\pi ia^2\sum_{n=0}^{\infty}\sum_k\varepsilon_n\cos n\phi\frac{N_n\left(\lambda_n^{(k)}\right)\exp\left(i\lambda_n^{(k)}|z|\right)}{D_n'\left(\lambda_n^{(k)}\right)}\end{array}\right]. \tag{53}$$

The expression in equation (53) is significantly more complex than the corresponding integral for a metal cylinder and dipole source in an unbounded medium. In the unbounded medium there are no waveguide modes so there are no poles. It is an important check to show that equation (53) reduces to the expression for the branch cut integrals derived by *Freedman* [2015] for the case of a single-layer unbounded medium. The magnetic field in an unbounded medium is obtained from equation (53) by letting $\gamma_1 = \gamma_2 = \gamma$ (or equivalently $k_1 = k_2 = k$).

The calculations are too lengthy to present here; however, it is worthwhile to provide the reader some of the steps. In equations (40)–(43) we first set $\gamma_1 = \gamma_2 = \gamma$ and $k_1 = k_2 = k$, which simplifies the equations. Next we replace the Hankel function and its derivative by modified Bessel functions by using equation (21b) in *Freedman* [2015]. Next we recall equations (21), (22), (26), and (27) and combine terms by using the Wronskian for modified Bessel functions. Some lengthy but straightforward algebra leads to the equation,

$$\frac{N_n^{(+)}}{D_n^{(+)}} = \frac{ixK_n(ix)}{K'_n(ix)} = -\frac{xH_n^{(2)}(x)}{H_n^{(2)'}(x)},$$ (54a)

where the last equality in equation (54a) follows from equation (21b) as noted above. Similar steps can be applied to equations (48)–(51) if one uses equation (21a) in *Freedman* [2015]. One then finds that

$$\frac{N_n^{(-)}}{D_n^{(-)}} = \frac{-ixK_n(-ix)}{K'_n(-ix)} = -\frac{xH_n^{(1)}(x)}{H_n^{(1)'}(x)}.$$ (54b)

The algebraic sign difference in the argument of the modified Bessel functions in equations (54a) and (54b) comes from the double-valued square root function $t(x) = \sqrt{-x^2} = \pm ix$ in equation (45), which is equal to $+ix$ on the branch line γ_{2+} and is equal to $-ix$ on the branch line γ_{2-}. Note that the radius b of the interface separating the two media is an irrelevant parameter in this limit and drops out of the calculations when deriving equation (54a) and (54b). Substituting equations (54a) and (54b) into equation (53) finds for a single-layer medium that

$$H_z(a, \phi, z) = \frac{-iM_o}{2\pi^2 a^3} \sum_{n=0}^{\infty} \varepsilon_n \cos n\phi \int_0^{\infty} \frac{x^2 \exp\left(i\sqrt{(ka)^2 - x^2}|\bar{z}|\right)}{\sqrt{(ka)^2 - x^2}} \text{Im}\left[\frac{H_n^{(1)}(x)}{H_n^{(1)'}(x)}\right] dx,$$ (55)

which is identical to equation (28) in *Freedman* [2015] for an unbounded single-layer problem if the change of variables $x = ua$ is made in equation (55). It is worth noting that the only complex quantity in the integrand of equation (55) is the argument of the exponential function. The Hankel functions in the integrand in equation (55) have real arguments and can be easily computed. This is not the case for the more complex two-layer medium integrand because the functions $F_{1,n}(x), \cdots, F_{4,n}(x)$ in the integrand of equation (53) contain modified Bessel functions with complex arguments. In addition to the more complex branch line integrals, the poles of the integrand in equation (29) must be found and their residues computed in order to compute the magnetic field in equation (53).

The integrands of the branch line integrals in equation (53), in contrast to the integrand of the real-axis integral in equation (29), are convergent and decay to zero exponentially for large values of the integration variable x and therefore are useful for practical numerical computations. We used the branch line integrals in equation (53) to study the effects of a standoff layer on the phase shifts and attenuations of the complex magnetic field $H_z(a, \phi, z)$. The complex branch line integrals were integrated by using Simpson's rule with automatic interval halving applied until the convergence condition was achieved. The computation of the branch line integrands requires a summation over the azimuthal index n in equation (53) for each value of the integration variable (x). The terms in the sum require computation of modified Bessel functions $K_n(z), I_n(z)$ and their derivatives with respect to a complex argument z. The number of azimuthal modes required for the convergence of the sum over n is problem-dependent. For a study of an EM wave propagation logging tool operating at 1.1 GHz the author found that the number of terms needed for convergence of the sum was less than 100. For most of the cases studied the integrand in equation (53) is smooth and well behaved like the example shown in Figure 2. The computer code used to compute the integrand was written in Fortran by using double-precision floating point computations. Nevertheless, for some cases, especially for thinner standoff layers (e.g., $(b - a) < 0.5$ cm), the integrands were spiky as if perturbed by numerical noise, which is believed to be caused by computer round-off errors. In an attempt to reduce the errors for the
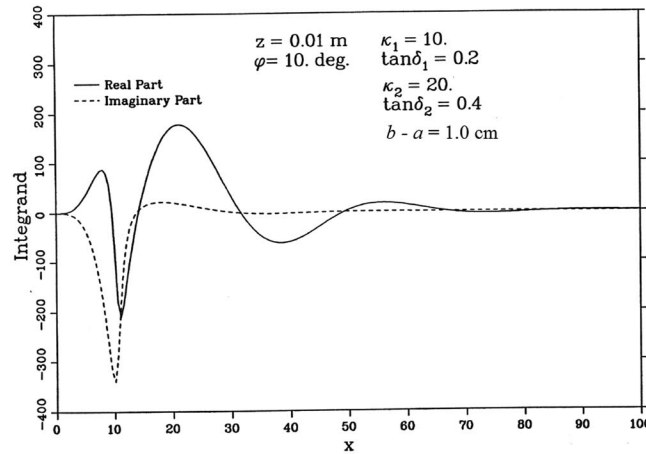
Figure 2. The real (solid) and imaginary (dashed) parts of the complex branch cut integrand in equation (53) plotted versus the dimensionless integration variable x. The transmitter frequency is 1.1 GHz, and the cylinder radius is 0.1016 m. The integrand is smooth and decays rapidly to zero as the integration variable increases. In this example the z coordinate was chosen to be close to the transmitter to show that the integrand decays quickly even for small z values. The relative dielectric constants and loss tangents of the two layers and the thickness of layer 1 are shown.

problematic cases the branch line integrands were combined algebraically and the combined integrand was computed. The combined integrand exhibited the same noise as the original coding of the two separate branch line integrals. The other possible cause of the noisy integrands might be errors in the computations of $K_n(z)$ and $I_n(z)$ for some orders of (n) and for some complex arguments in equation (53). The modified Bessel functions were computed by using commercial IMSL subroutines.

4. Computation of the Residues of the Poles in the Real-Axis Integrand

The poles correspond to excitations, which are analogous to bound states in quantum mechanical scattering theory. In the EM problem the poles are waveguide modes or trapped waves that can propagate in the standoff layer. Mathematically, these poles correspond to the discrete eigenvalue spectrum of a differential operator. Here the differential operator is the Helmholtz wave equation with dissipation. Mathematicians have discussed various general properties of the eigenvalue spectra of Sturm-Liouville-type differential operators although usually for lossless systems [*Titchmarsh*, 1958]. Also, bounds can be derived for the pole locations for planar problems [*Chew*, 1990, pp. 114–117]. A similar mathematical proof can probably be derived for bounds on the pole locations for the azimuthally asymmetric problem treated here; however, the author does not attempt a mathematical proof but instead provides a heuristic physical argument to place bounds on the pole locations.

To compute the residue sum in equation (53), first the poles must be found, i.e., solve the equation:

$$D_n\left(\lambda_n^{(k)}\right) = 0 \qquad (56)$$

for $n = 0, 1, 2, \cdots$, where $D_n\left(\lambda_n^{(k)}\right)$ is defined in equation (31) for $n > 0$ and in equation (33) for $n = 0$. The integer index k in equation (56) accounts for the existence of multiple poles for a given azimuthal mode (i.e., index n). We use a complex Newton's method to iteratively solve equation (56) by using a judiciously chosen grid of initial search points, as discussed in the next section. First, we give a heuristic physical argument that was used to anticipate bounds on the pole locations in the complex λ-plane. Physically, the poles $\lambda_n^{(k)}$ correspond to the spectral wave numbers of modes that are excited in the standoff layer (e.g., layer 1). It can be argued that the poles will be in the first and third quadrants of the complex λ-plane and are bounded by the hyperbolas $\lambda'\lambda'' = k_1'k_1''$ and $\lambda'\lambda'' = k_2'k_2''$. That is, the wave numbers of the waveguide modes are expected to be between those of the standoff layer (medium 1) and the unbounded layer (medium 2). In the limit as the standoff layer thickness approaches zero, the poles should approach the hyperbola $\lambda'\lambda'' = k_2'k_2''$. In the opposite limit of a thick standoff layer, the poles should approach the hyperbola $\lambda'\lambda'' = k_1'k_1''$. The modes that contribute to the magnetic field in equation (53) are the propagating modes that lie closest to the real axis. As shown in the following, many of the modes can have vanishingly small residues and are not of practical importance. The nonpropagating modes are often referred to as evanescent modes.

The zeroes of $D_n(\lambda)$ are found by using the complex Newton's method, which involves an iterative solution of the following recursion formula:

$$\lambda_n^{(k)^{(m+1)}} = \lambda_n^{(k)^{(m)}} - \frac{D_n\left(\lambda_n^{(k)^{(m)}}\right)}{D_n'\left(\lambda_n^{(k)^{(m)}}\right)}, \qquad (57)$$

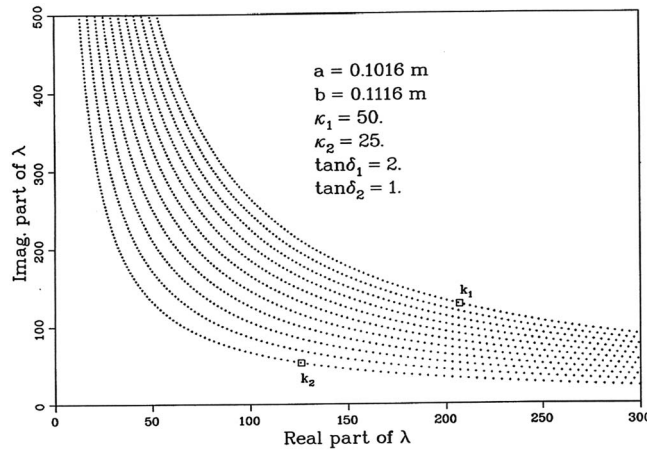**Figure 3.** Lattice of initial search points used in equation (57) to locate the $n = 0$ poles for the example in Figure 4.

where $m = 0, 1, \cdots$ is an iteration index and $n = 0, 1, 2 \cdots$ are the indices of the azimuthal modes. The prime denotes the derivative with respect to λ of $D_n(\lambda)$ in equation (31) for $n > 0$ and in equation (33) for $n = 0$. The derivatives can be performed analytically so that numerical differentiation is not necessary in equation (57). In the next section we discuss the details of the pole search algorithm.

4.1. Pole Search Algorithm

The following algorithm was developed and used to locate the poles:

Step a: Use a fine grid of points as initial values $\lambda_0^{(k)^{(0)}}$ to locate all the $n = 0$ poles.

Each of the $n = 0$ poles found is associated with a branch labeled by $k = 1, 2, 3, \cdots$. On locating a pole, a check is made to determine whether or not the pole is unique. If the pole has already been found then it is discarded. **Step b:** Use the $n = 0$ poles for $\lambda_0^{(k)}$, found in **Step a** as starting points in equation (57), to find the $n = 1$ poles for $\lambda_1^{(k)}$, then use the poles $\lambda_1^{(k)}$ as starting points to find the $n = 2$ poles for $\lambda_2^{(k)}$ and etc. A computer program was written to automatically generate the search grid, locate the poles, and perform the sum over residues in equation (53). An example of a search grid is shown in Figure 3, and a single branch of poles (i.e., $\lambda_n^{(1)}$ for $n = 0, 1, 2, \cdots$) found by using the pole search algorithm is shown in Figure 4. It is interesting to note that in this example the standoff layer thickness is 1.0 cm, $\kappa_1 = 50$, and $\tan \delta_1 = 2$, and for $f = 1.1$ GHz, the one-quarter wavelength is approximately 0.76 cm, which is less than the layer thickness. We found that if the layer thickness is decreased to less than one-quarter wavelength, e.g., to 0.70 cm, then the poles disappeared and the guided modes were not excited. Another interesting feature of the pole spectrum in Figure 4 is that there is a gap or forbidden region in the spectrum that occurs for this example when the pole $\lambda_{59}^{(1)}$ reaches the branch cut (i.e., the hyperbola passing through k_2). The next pole $\lambda_{60}^{(1)}$ on the branch is displaced relatively far from $\lambda_{59}^{(1)}$, which is reminiscent of gaps in the energy spectrum of electrons in crystalline solids. In solids the gaps are due to reflection of the electrons from the Brillouin zone boundaries as a result of the absence of translational invariance in the crystal lattice. Here the branch cut represents a boundary in the complex λ-plane, which if crossed would lead to solutions on the nonphysical Riemann sheet and therefore are not allowed. In general, there are a denumerably infinite set of poles; however, the residue summations in equation (53) have been found to be rapidly convergent for the problem parameters studied by the author
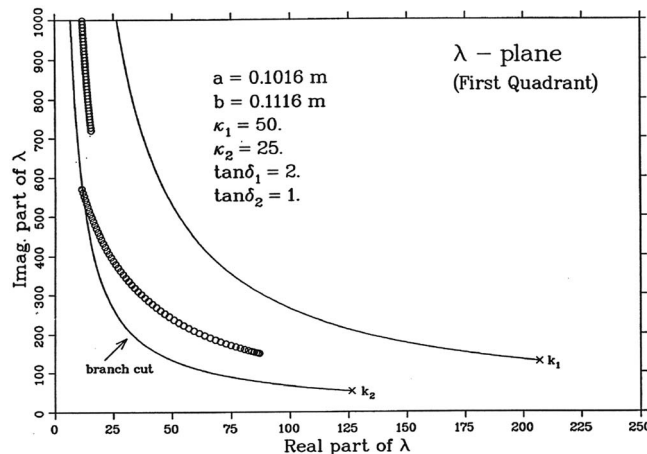

Figure 4. Single branch of poles found for a 1 cm thick standoff layer. Note the gap in the pole spectrum near the branch cut.

so that only a relatively small number of poles contribute significantly to the sums. Figure 5 shows a plot of the imaginary part of the residue R_n'' versus the real part R_n' for the poles of order $n = 0, 1, 2, \cdots$, which are shown in Figure 4. Observe that both the real and imaginary parts of the complex residues rapidly spiral toward vanishingly small values. It has been found for small standoff thicknesses (e.g., $b - a \approx 1.0$ cm) that the branch cut integrals totally dominate over the residue contributions; however, as the standoff layer thickness is increased eventually the branch cut integral contribution becomes negligibly small and the waveguide mode
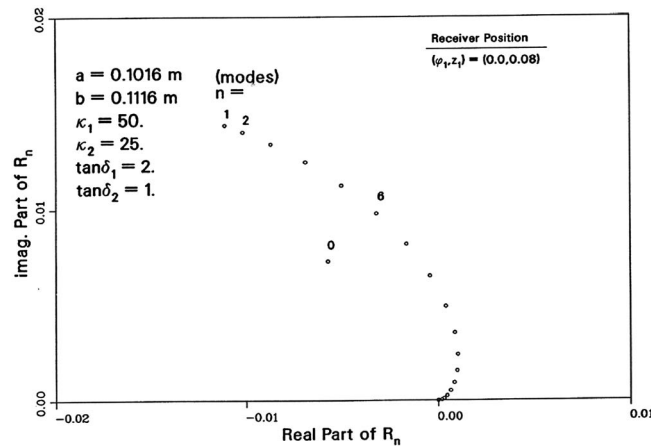
Figure 5. Plot of the real and imaginary parts of the residues for the poles in Figure 4. Observe that for a 1.0 cm thick standoff only a few poles have nonzero residues; i.e., the magnetic field on the cylinder surface is effectively determined by the branch line integrals.

contributions dominate. An example for a 10 cm thick standoff layer for which the dominant magnetic field at the receivers is derived from the pole contributions (i.e., from the sum of the residues) in equation (53) is subsequently discussed. Moreover, as the standoff layer thickness is increased, multiple branches of poles exist. For example, if the standoff layer thickness for the situation depicted in Figure 4 is increased from 1.0 cm to 3.0 cm, then the four branches of poles shown in Figure 6 are found.

4.2. Checks on the Pole Search Algorithm and Residue Summation

It is comforting to check the pole search algorithm. A simple check on the $n = 0$ poles found in **Step a** of the previous section is easily performed to show (e.g., see Figure 4) that for the pole locations in the complex λ-plane the conditions $|\gamma_j a| \sim 20$ for $j = 1, 2$ so that the asymptotic expansions [*Olver*, 1965] can be used for the Bessel functions and their derivatives in equations (33), (26), and (27). It is found from equation (33) that

$$D_0(\lambda) \sim -\frac{1}{\gamma_1 \sqrt{ab}}\left[\sinh(\gamma_1(b-a)) + \frac{\gamma_1}{\gamma_2}\cosh(\gamma_1(b-a))\right]. \tag{58}$$

The pole search algorithm including the search grid and the complex Newton's method was used to find the zeroes of equation (58) that correspond to the $n = 0$ poles $\lambda_0^{(k)}$. For the cases studied the pole locations or zeroes of equation (58) agreed to several decimal places with the values of $\lambda_0^{(k)}$ found by using the more general expression given in equation (33). This provides a good check on the Bessel function computations and on the pole search algorithm. It is also interesting to note that the expression in equation (58) is identical to the dispersion relation for TE surface waves guided along a dielectric slab backed by a metallic ground plane [*Mittra and Lee*, 1971]. This is not too surprising because the asymptotic expansion is equivalent to a planar problem limit where the cylinder radius becomes much larger than a wavelength.
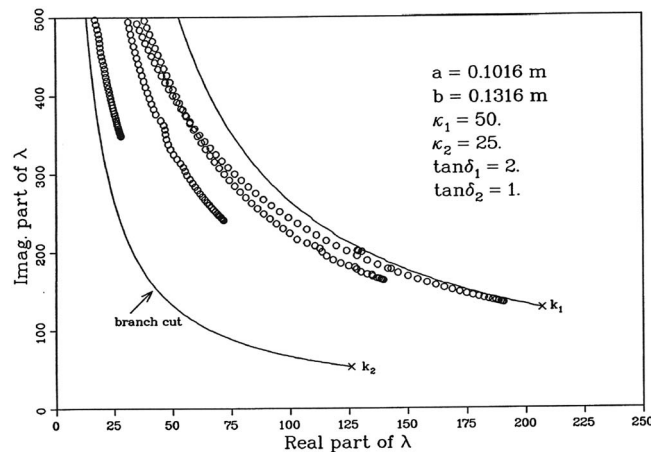

Figure 6. Four branches of poles found for a 3 cm thick standoff layer. The propagating waveguide modes have poles that lie closest to the real axis and propagate with wave numbers close to that of layer 1.

As the thickness of the standoff layer increases beyond the depth of investigation of the transmitted signal, the pole contributions to the logging tool responses are expected to become dominant. The depth of investigation is of the order of the skin depth of the EM fields in the standoff medium. In the limit of a standoff layer thickness greater than the depth of investigation most of the contribution to the tool response should come from the waveguide modes with negligible contribution from the branch cut integrals. To demonstrate this fact and to check the residue summation we computed the response of a 1.1 GHz microwave dielectric logging tool in a two-layered medium. The tool has a longitudinally
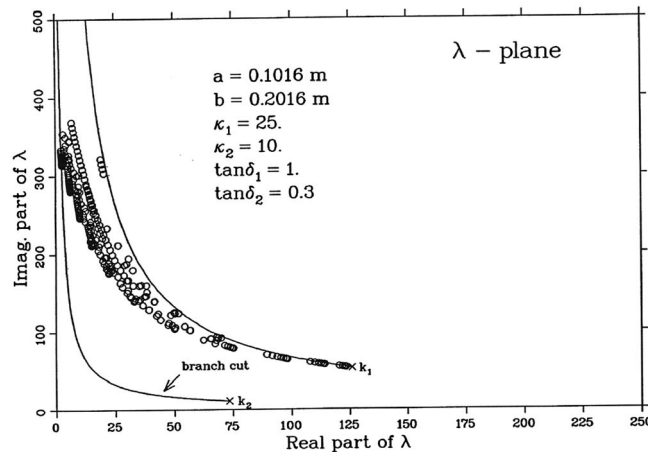
Figure 7. Poles for a 10 cm thick standoff layer. Essentially, all of the magnetic field is derived from the standoff medium (i.e., from summing the pole residues).

oriented point magnetic dipole transmitter and two receivers located on a metal cylinder with radius $a = 0.1016$ m (4 in.). The transmitter is located on the cylinder at $(a, \phi, z) = (0.1016, 0.0, 0.0)$, and the two receivers are located on the cylinder at $(a, \phi_1, z_1) = (0.1016, 0.0, 0.08)$ and $(a, \phi_2, z_2) = (0.1016, 0.0, 0.12)$. The measured tool responses are the phase shifts and attenuations of the complex magnetic field in equation (53) between the receivers. The phase shifts and attenuations between the receivers on the cylinder surface can be computed using formulas (7) and (9) in *Freedman and Vogiatzis* [1979] for computing phase shifts in radians and attenuations in decibels per meter (dB/m), respectively.

The following test of the pole search algorithm and residue summation was performed. The response of the logging tool was computed for a two-layer medium with a standoff layer thickness of 10 cm. The EM properties of the standoff layer are shown in Figure 7. A measure of the depth of penetration or skin depth δ of the transmitted EM field was estimated by using the imaginary part of the complex propagation constant of the standoff layer, i.e., $\delta = \left(k_1''\right)^{-1}$. Using the properties of the standoff layer shown in Figure 7 finds $\delta \approx 7$ cm at 1.1 GHz. Therefore, for a standoff layer thickness of 10 cm the phase shift and attenuation should be dominated by the waveguide modes that are trapped in layer 1.

The pole search algorithm located 15 branches (i.e., $k = 1, 2, 3 \cdots, 15$) and the 263 distinct poles shown in Figure 7. The orders of the 263 poles were $n = 0, 1, 2, \cdots, 49$. Poles with higher orders were not included in the search. The magnetic fields at the two receivers were computed by summing the residues in equation (53). The computed phase shift in degrees and the attenuation from the residue summation were 288° and 656 dB/m, respectively. As a check on these results the magnetic fields at the receivers were computed by using the solution in equation (55) for the one-layer problem with the same EM properties as the standoff layer (i.e., $\kappa_1 = 25$ and $\tan \delta_1 = 1$). The computed phase shift and attenuation for the one-layer medium were 290° and 635 dB/m, respectively. The two phase shifts agree to within 0.7% and the two attenuations to within about 3%. The close agreement of these results is an important check on the accuracy of the pole search algorithm and the residue summation computation.

References

Chew, W. C. (1983), The singularities of a Fourier-type integral in a multicylindrical layer problem, *IEEE Trans. Antenn. Propag.*, AP-31(4), 382−387.

Chew, W. C. (1990), Planar layered media, in *Waves and Fields in Inhomogeneous Media*, pp. 114−121, Van Nostrand and Reinhold, New York.

Freedman, R. (2015), Derivation of magnetic fields on a metal cylinder excited by longitudinal and transverse magnetic dipole transmitters: I. Cylinder in unbounded dissipative dielectric medium, *Radio Sci.*, 50, 941−955, doi:10.1002/2014RS005645.

Freedman, R., and J. P. Vogiatzis (1979), Theory of microwave dielectric logging using the electromagnetic wave propagation method, *Geophysics*, 44(5), 969−986, doi:10.1190/1.1441048.

Hizem, M., H. Budan, B. Devillé, O. Faivre, L. Mossé, and M. Simon (2008), "Dielectric dispersion: new wireline petrophysical measurement (paper 116130), Proc. Soc. Petr. Eng. Ann. Tech. Conf. and Exhibition, Denver, Co. pp. 1−21.

Mittra, R., and S. W. Lee (1971), Wiener-Hopf techniques, in *Analytical Techniques in the Theory of Guided Waves*, pp. 121, MacMillan, New York.

Olver, F. W. J. (1965), Bessel functions of integer order, in *Handbook of Mathematical Functions*, edited by M. Abramowitz and I. A. Stegun, pp. 358–433, Dover, New York.

Stratton, J. A. (1941), The electromagnetic potentials, in *Electromagnetic Theory*, pp. 23−32, McGraw-Hill, New York.

Titchmarsh, E. C. (1958), *Eigenfunction Expansions Associated With Second Order Differential Equations*, Oxford Univ. Press, Oxford, U. K.

Wait, J. R. (1987), General solution for excitation by slotted aperture source in conducting cylinder with concentric layering, *IEEE Trans. Microwave Theory Tech.*, 35(3), 321–325, doi:10.1109/TMTT.1987.1133645.